Journal of Advanced Joining Processes 13 (2026) 100361

Contents lists available at ScienceDirect

Journal of Advanced Joining Processes

journal homepage: www.sciencedirect.com/journal/journal-of-advanced-joining-processes

Influence of secondary aluminum content on casting and weldability of high pressure die cast materials for sustainable automotive body concepts

Dirk Dittrich [a,*], Dirk Lehmhus [b], Marco Haesche [b], Leonardo Fernandes Gomes [b], Christoph Pille [b], Axel Jahn [a], Linda Ullmann [a], Charlotte Graner [a]

[a] Department of Joining, Fraunhofer Institute for Material and Beam Technology IWS, Winterbergstraße 28, 01277 Dresden, Germany
[b] Department of Casting Technology, Fraunhofer Institute for Manufacturing Technology and Advanced Materials IFAM, Wiener Straße 12, 28359 Bremen, Germany

ARTICLE INFO

Keywords:
Primary and secondary aluminum alloys
High-pressure die casting
Dynamic beam oscillation
Laser welding
Mechanical properties
Fatigue

ABSTRACT

Sustainability is becoming increasingly important in vehicle production. The e-mobility transition has shifted the CO_2 footprint from use to production phase, where secondary aluminum alloys in structural castings are known to offer significant CO_2 reduction potential. However, accumulation of copper, iron, manganese and zinc and the hydrogen content in the melt pose major challenges for casting and subsequent joining processes. In laser welding, dynamic modulation of intensity distributions in the weld pool can overcome the latter issue. In experimental studies covering high pressure die-cast AlSi10MnMg alloys with secondary material content levels ranging from 0 wt.-% and 58 wt.-% to 89 wt.-%, castability and weldability were investigated and the structural and mechanical properties of the joint determined. The results contribute to the optimization of sustainable car body production, providing a path towards cost-effective differential lightweight design solutions as economically, technologically and ecologically competitive alternatives to large-scale casting technologies (GigaCasting).

Introduction

Aluminum alloys are particularly well-suited for use in lightweight design due to their combination of properties and their availability, as evidenced by their widespread use in the manufacture of car body structures (Prieto et al., 2020; Letyagin et al., 2024). High-pressure die casting (HPDC) of light metal alloys in particular enables the fabrication of a wide range of complex automotive parts, including thin-walled structures and components featuring delicate ribs. Primary alloys frequently used in high quality aluminum casting are obtained from mining ores like bauxite, typically relying on the Bayer and Hall-Heroult processes for extracting the metal. The high energy consumption associated with these manufacturing routes contributes directly and indirectly to climate change (Rohwer et al., 2024). One strategy for reducing emissions involves the use of secondary alloy fractions, aiming at the highest possible recycled content in the final material. Depending on process and energy source, the recycling process requires far less energy than primary production – an exemplary calculation focusing on the Chinese aluminum industry relates 77,547 MJ of direct energy consumption per ton for the latter, while recycling of the same amount of aluminum accounts for only 8,612 MJ. Needless to say, the carbon footprint follows the same trend, with primary material production releasing 15,947 kg $CO_{2\text{-eq}}$ per ton of aluminum based on a life cycle perspective ranging from bauxite mining all the way to ingot casting, while the recycling path ends up at a mere 845 kg $CO_{2\text{-eq}}$ (Peng et al., 2022). Obviously, such figures depend heavily on local energy mix, but the tendency and thus the advantage of secondary over primary aluminum are equal anywhere in the world. Compared to the global emissions currently associated with primary aluminum alloy provision, following a recycling path can save over 100 million tons of carbon dioxide (CO_2) annually (Rohwer et al., 2024; International Aluminium, 2025). In conjunction with the Paris Climate Agreement and the goal of achieving net zero carbon emissions by 2050, the development of strategies to reduce the carbon footprint has become essential (Rohwer et al., 2024). Consequently, the automotive industry is shifting its focus to the use of secondary instead of primary aluminum (Rohwer et al., 2024; De Caro et al., 2023). Evaluating the consequences of fabricating cast automotive components like car body and powertrain parts or battery cases from secondary materials thus becomes a necessity for approaching the aim of climate-neutral production (Rohwer et al., 2024; De Caro et al., 2023; Bleicher et al., 2025). Currently, a trend towards ever-larger cast aluminum components can be observed for which terms

* Corresponding author.
E-mail address: dirk.dittrich@iws.fraunhofer.de (D. Dittrich).

https://doi.org/10.1016/j.jajp.2025.100361

Available online 28 November 2025

like Giga- or MegaCasting have been coined (Burggräf et al., 2024). Such tendencies will likely lead to an increase in the aluminum content across all vehicle classes - despite the fact that e-mobility eliminates classic cast aluminum components like engine blocks or oil pans (Lehmhus, 2022). However, large scale castings are not necessarily a lightweight design solution, since they may violate the paradigm of using the right material in the right place, representing an integral rather than differential approach towards automotive body design (see Fig. 1). In a casting context, differential structures may be achieved by means of compound casting (Lehmhus, 2024), or via suitable joining processes. Among the latter, Laser welding has developed into an established technology in the automotive industry for realization of multi-part, differential concepts. Nevertheless, there is ample room for research: While Laser welding of cast, and especially high pressure die cast (HPDC), aluminum remains a challenge in general, the need to reduce CO_2 emission raises the additional question whether differential structures incorporating cast parts can also be based on secondary aluminum alloys. Beyond the focus on lightweight design, compared to GigaCasting, this could provide additional benefits in terms of repairability of structures. Furthermore, from an economic point of view, the differential approach could allow foundries to compete with GigaCasting and profit from the trend towards large structural castings without having to shoulder the considerable investment in equipment this technology affords, but rely instead on their existing, conventional HPDC systems which provide more flexibility than the oversized GigaCasting appliances.

The main point of concern regarding the weldability of secondary aluminum alloys is the presence of elevated quantities of undesirable elements such as iron, copper and zinc, which are known to accumulate in the course of the recycling process, and which cannot easily be removed (De Caro et al., 2023; Bleicher et al., 2025; Ashtari et al., 2012). In particular, in typical structural alloys like AlSi10MnMg, the increase in iron content from 0.02-0.15 wt.-% to 0.3-0.5 wt.-% is considered critical, as it affects the microstructure and thus also the mechanical properties (Ashtari et al., 2012; Mikolajčika et al., 2023). Naturally, the altered chemical composition may also influence subsequent manufacturing steps such as casting and laser beam welding. A possible increase in the porosity of die cast material is also a potential consequence of an increased iron content, as plate-shaped Al_5FeSi phase can hinder feeding by blocking the flow of the melt during solidification (Mikolajčika et al., 2023).

Welding of high pressure die cast aluminum components is widely regarded as a technically demanding process. The potentially high gas content of such castings and the fact that pores already present after casting can be under high pressure may lead to severe porosity in the weld seam, as well as the random ejection of the melt (Dittrich, 2019). This results in reduction of the cross-section's rigidity and in some cases, insufficient joint quality. In order to overcome these obstacles, a technology based on dynamic laser beam shaping was developed for the purpose of welding the wrought aluminum alloy AlMgSi0.5 to the cast aluminum material AlSi10MnMg. This approach has been demonstrated to enhance the quality of the resulting weld seam.

Experimental procedure

The experimental study aims to establish the impact of recycled aluminum content on the castability and weldability of AlSi10MnMg in combination with AlMgSi0.5 (EN AW-6060) in a precipitation hardened T66 state. The materials used, the casting equipment and the welding hardware are described in more detail below.

Materials

In order to determine the influence of recycled aluminum on castability and weldability, commercial aluminum alloys of AlSi10MnMg and with secondary material content levels of 0, 58 and 89 wt.-% were used to cast plates used as welding partner for the wrought AlMgSi0.5 alloy. The two alloys with no and lower level of recycled material were supplied by Aluminium Rheinfelden (trade name Silafont-36® for the primary material, Aluminium Rheinfelden Alloys GmbH, Rheinfelden, Germany), while the alloy containing 89 wt.-% of recycled aluminum stems from Raffmetal (SILVAL-10®, Raffmetal S. p. a., Casto, Italy). All alloys were supplied as commercial ingots and melted in an electric resistance furnace at 740 °C in a 220 kg capacity silicon carbide crucible. Different amounts of the master alloy Al-10Sr and pure Mg ingots were added to the melt in order to obtain the desired alloy composition (adjustment of Sr and Mg content to similar levels across all alloys, see section 2.2). The chemical composition of all alloys was analyzed using an ARL 3460 emission spectrometer (Thermo Fisher Scientific Inc., Waltham, USA) and found to be in accordance with the alloy designation EN AC-43,500, DIN EN standard 1706:2021 (DIN EN 1706, 2021). The proportion of melted scrap results in an accumulation of the accompanying elements it contains, thus influencing the chemical composition, as can be seen in Table 1 with respect to the Cu, Fe and Zn content level.

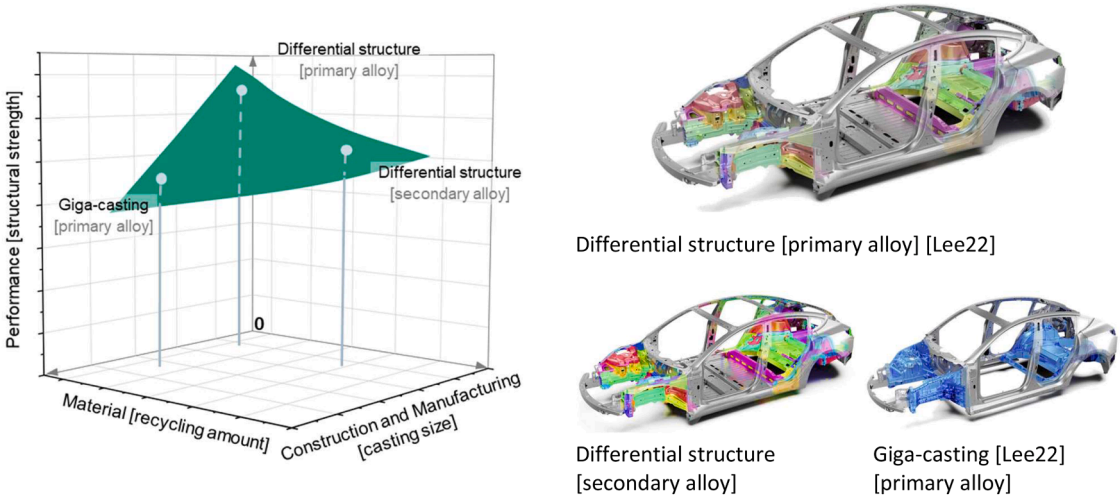

Fig. 1. Illustration of the possible effects of GigaCasting and secondary alloy use on part performance: GigaCasting today mainly relies on primary alloys and may underperform in terms of lightweighting, as process-related rather than structural requirements may control local thickness and material properties may degenerate with flow length. Differential structures may thus fare better even if deductions accounting for secondary materials properties are necessary. Adapted: (Lee-Jones, 2022).

Table 1
Chemical composition of the primary and secondary alloys under scrutiny as well as the wrought alloy used as welding partner. Casting alloy composition measurements refer to the second day of the three-day casting campaign in each case.

Alloy variants		Chemical composition in wt.-%														
		Si	Fe	Cu	Mn	Mg	Cr	Zn	Ti	Sr	Ni	Pb	Sn	Sb	Ca	P
AlSi10MnMg	**100 % primary**	**10.11**	**0.084**	**0.0022**	**0.504**	**0.271**	**0.001**	**0.002**	**0.007**	**0.019**						
	58 % secondary	**10.17**	**0.14**	**0.020**	**0.617**	**0.269**	**0.004**	**0.009**	**0.061**	**0.020**	**0.008**	**0.002**	**0.001**	**0.0003**		
	89 % secondary	**9.548**	**0.34**	**0.026**	**0.458**	**0.269**	**0.011**	**0.025**	**0.086**	**0.019**	**0.005**	**0.004**	**0.001**	**0.0003**	**0.0006**	**0.0018**
AlMgSi0.5		**0.431**	**0.151**	0.0013	0.0163	**0.479**	0.00054	0.0041	0.0068		0.0051	0.0011			0.00011	

Chemical elements correction and melt quality casting

As the aim of the present investigation was to evaluate the influence of the recycled content on welding behavior, the chemical composition was not altered, with the exception of magnesium and strontium. Since the magnesium content can influence ductility and strength of AlSi10MnMg alloys, an average Mg content of approx. 0.27 wt.-% was set for all three casting alloy variants before the start of the casting tests (Aluminiumlegierungen - Qualität für die industrielle Verarbeitung). Strontium was used to refine casting alloys by modifying eutectic silicon. It is already present in sufficient quantities in all casting alloys, but can burn off during the melting process, or during prolonged holding times, necessitating its re-addition. The target value was an Sr content of approx. 150 to 250 ppm. After adding the necessary chemical elements, the melt was purified by rotor degassing until a density index of < 2 % was achieved. The latter is a technological measure which provides information about the melt quality. To determine its value for a given melt, two identical samples with a weight of approx. 80 g to 100 g were cast. One of these was solidified under normal atmospheric pressure, the other at a reduced pressure of 80 mbar. The density index was then calculated as the difference between the density of these two samples in relation to the density of the atmospheric sample multiplied by 100 % (Dichte-Index, 2025). Its value is an indication of the gas content of the melt. Furthermore, since the dissolved gases often nucleate and attach to non-metallic impurities during solidification, a low density index indirectly hints at a low level of non-metallic impurities.

HPDC experiments

The die casting experiments were carried out at the Fraunhofer IFAM technical center using a real-time controlled Frech DAK 250 cold-chamber HPDC machine featuring a clamping force of 290 t. The machine is equipped with a Fondarex (Fondarex SA, St-Legier, Switzerland) vacuum system and an Electronics® (Electronics GmbH, Neuhausen, Germany) process data measurement system for monitoring the casting process. The most important casting parameters, which were kept constant across all alloy variants, are listed in Table 2.

The process parameters were recorded, allowing to link, for each casting, component quality to the corresponding process data. Ensuring data traceability and maintaining reproducibility of parameters during the HPDC process such as plunger speed, intensification pressure, melt and die temperatures are essential aspects for maintaining quality over a series of parts. To facilitate real-time monitoring and gather additional information from within the cavity, sensors were strategically placed in the die to monitor the conditions at the die's surface, which is in direct contact with the melt during filling and solidification prior to ejection. Specifically, two sensors (S1 and S2) designed to measure temperature and pressure were installed in the movable half of the die. The signals acquired by these sensors were collected and are illustrated in Fig. 2. The mold used in this study produces a dogbone- and a plate-shaped specimens per shot, the latter measuring 150 mm x 40 mm x 3 mm. These were subsequently employed for welding trials conducted at Fraunhofer

Table 2
List of the most important manufacturing parameters for producing the high pressure die cast samples.

Die-casting equipment and process parameters	Value
Melt temperature	700 ± 10 °C
Mold temperature	190 ± 10 °C
1st phase plunger speed	0.26 m/s
2nd phase plunger speed	3.8 m/s
Intensification pressure	800 bar
Plunger diameter	40 mm
Vacuum support	Yes (Fondarex)
Release agent	Chemtrend SL 1697 S (1:70)
Release agent application	Manual application

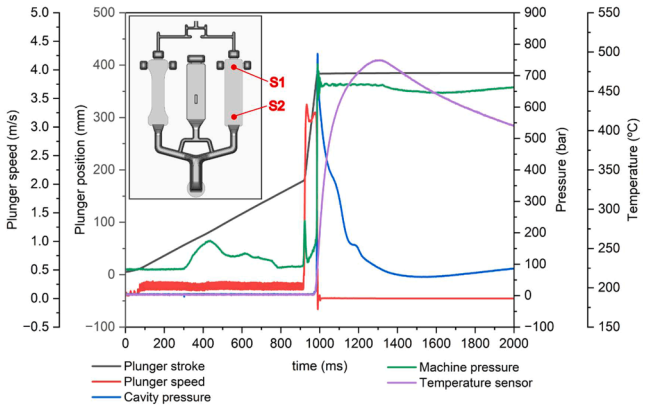

Fig. 2. Shot curve measured by Electronics® during the HPDC process. Machine pressure denotes the pressure acting on the melt at the plunger, while cavity pressure is the level recorded by the respective sensor S2.

IWS. The 3D model representing the movable and fixed part of the mold is depicted in Fig. 3.

Welding

To evaluate the laser weldability of primary and secondary aluminum die-casts, welding tests were carried out on a 5-axis CNC welding machine using up to 2 kW single-mode fiber laser and highly dynamic beam deflection optics. The laser processing head consists of a classic XY-scanner (welDYNA, Scanlab). The specifications of the laser equipment and optics can be found in Table 3.

This enables the display of so-called Lissajous Figures in the kHz range. This specific approach is necessary to overcome limitations caused by a static laser beam. The HPDC manufacturing method carries the risk of gas being entrapped within the cast product. As during solidification, the intensification pressure acts on the entrapped gas, the respective pores are characterized by a considerable internal pressure. If a casting containing such pores is heated up, the temperature increase will lead to a reduction in material strength which may suffice to let the pores expand, forming blisters on the surface of the part even if the solidus temperature is not exceeded. Conventional laser beam welding must naturally go beyond the *liquidus* temperature, when cutting any larger amount of pores will lead to welded joints with excessive porosity and, in some cases, severe ejection of the melt. By applying an optimized scan contour overlaid on the welding feed, the molten material can be effectively degassed, resulting in low porosity and fully sealed welded joints. A detailed description of the underlying interaction between the

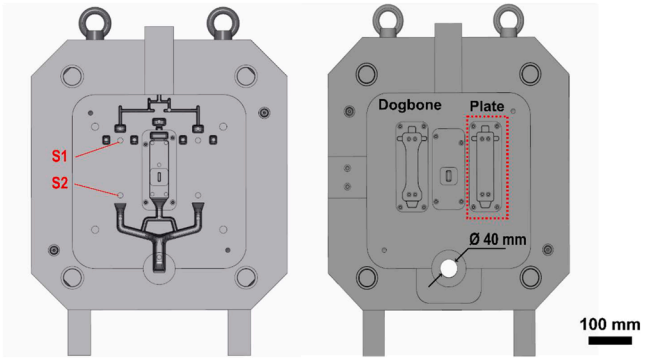

Fig. 3. CAD model of the HPDC die utilized in this study illustrating the fixed (right) and the movable die half (left). The temperature sensor (S1) and pressure sensor (S2), both embedded in the movable side, are highlighted in red. The image on the right hand side highlights the cavity employed in the present investigation, along with the plunger diameter of 40 mm.

Table 3
Overview of the equipment used in experimental trials.

Laser source / Scanner	YLS-2000-SM	welDYNA
Maximum laser power	2000 W	Osc. direction X and Y
Wavelength	1070 nm	Osc. frequency 0 … 4000 Hz
Beam parameter product	0.4 mm mrad	Osc. amplitude 0….0.15 mm
Core fiber diameter	30 µm	

material and the laser beam was provided by in situ X-ray experiments (Börner et al., 2021) based on experimental findings (Dittrich et al., 2017). An overview of the laboratory setup and the configuration of the welding tests for the procedures presented in this publication is shown in Table 4.

Preliminary investigations by Boerner et al. have highlighted the impact of oscillation parameters on weld seam quality during welding of hybrid joints between wrought aluminum alloys and copper (Börner et al., 2023). The aim of this study was to systematically analyze the relationship between beam path speed and weld seam quality, with a focus on understanding the effects on melt pool dynamics and keyhole formation. For comparison, reference welds were produced using static beam guidance with a spot diameter matching the one used in experiments with XY-oscillation. The investigation addresses the technical requirements with respect to the performance parameters identified and takes into account the normative principles of DIN EN ISO 13,919 (DIN EN ISO 13919-1, 2020). A cross-comparison between conventional laser beam welding with and without dynamic beam oscillation analyses the external appearance of the seam as well as the internal seam quality by means of a cross-section, using the example of the primary alloy examined, which was produced using HPDC.

To cover the multi-parameter matrix of process variables of the dynamic beam oscillation process (laser power, welding speed, focus position, amplitude and frequency), a test matrix was developed with the aim of obtaining lowest levels of pore formation and avoiding spatter. The welding parameters used are shown in Table 5. A circular contour was used for the oscillation ($\Delta\phi = \pi/2$; the radius of the circle corresponded to oscillation amplitude a_{xy}). The parameters were selected so that the influence of beam shaping (oscillation) and welding speed could be demonstrated.

Analysis and testing methods

Component quality was assessed using X-ray radioscopy. The X-ray testing was performed using a YXLON MU 2000 X-ray system (Comet Yxlon GmbH, Hamburg, Germany) equipped with a 160 kV X-ray tube. The adjusted X-ray voltage of 42 kV and the tube current of 3.60 mA in combination with the detector performance allowed the analysis of pores down to dimensions of approx. 250 µm.

To evaluate possible microstructural differences between three different AlSi10MnMg cast alloys with varying recycling content, flat microsections were prepared from selected components. The specimens for the metallographic sections were taken from the center (in terms of both area and thickness) of the welding or tensile test specimens. The microstructure of the different cast alloys was analyzed in an unetched state using an optical microscope (Leica DMRX, Wetzlar, Germany).

Metallographic techniques and computed tomography (CT) were primarily employed to evaluate the welding results. The non-destructive analysis of the laser-welded butt joints was conducted using X-ray computed tomography. A micro-CT system, equipped with an YXLON FXE-225.99 TwinHead X-ray tube and a Perkin Elmer XRD 1611 XP detector was used to achieve an image resolution of approximately 30 µm for the analyzed samples. This resolution enables reliable detection of defects or pores with an equivalent spherical diameter of approximately 100 µm or larger. A test voltage of 220 kV was applied to ensure adequate material penetration. In addition, the microstructure of the butt joints was analyzed using optical microscopy (OLYMPUS GX51),

Table 4
Overview of technical setup to perform experimental laser welding trials.

Sketch of scanner for dynamic beam oscillation	CNC-machine including, laser, scanner optics, clamping device and PLC control unit	Experimental configuration
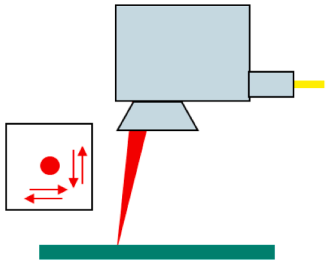 Technical data: - up to 4 kHz scanning frequency - up to 4 kW laser power - amplitude up to 0.3 mm	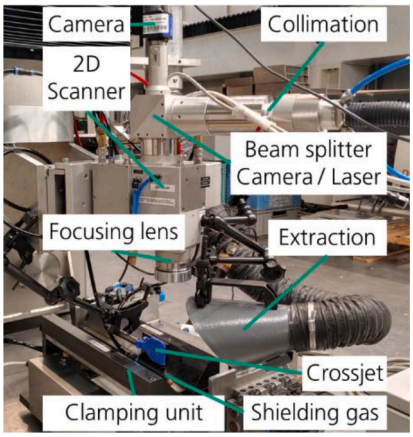	

Technical data
: up to 4 kHz scanning frequency
- up to 4 kW laser power
- amplitude up to 0.3 mm

Table 5
Welding parameter range for the reference laser welding process using static beam guidance and for dynamic beam oscillation as well as material combinations covered by the experiments.

Laser welding parameter	range for static beam guidance	range for dynamic beam oscillation	Material configurations for welding trials, according to Table 1 – AlMgSi0.5 vs. …
P_L in W	1 300 to 12 000	900 to 1000	A: primary AlSi10MnMg
v_s in m/min	1.5 to 10.0	0.6 to 1.2	B: 58 wt.-% secondary AlSi10MnMg
f_{xy} in kHz	0	4	C: 89 wt.-% secondary AlSi10MnMg
a_{xy} in mm	0	0.15	
$\Delta\phi$ in rad	0	$\pi/2$	

and local mechanical properties were assessed through hardness mapping (HV 0.1) using a LECO AMH55 system. The pores examined in the weld seam volume examined were analyzed in accordance with typical standards used in automotive engineering. Only pores with a diameter greater than 0.4 mm are identified and used for the calculation.

Tensile tests were conducted to establish the mechanical performance of the cast materials. Further experiments of this type focused on the characterization of the mechanical properties of the welded joints. Subject to these latter tests were the CT-examined samples. Mechanical testing was performed using an Inspect Table 50 kN testing machine equipped with a video extensometer (ONE1-M5). The tensile specimens were consistently tested in the same orientation and were extracted from the welded plates via laser cutting, see Fig. 4. In contrast, specimens for base material characterization were cut from castings originating from the dogbone cavity of the HPDC die used in sample production.

In addition to quasistatic tensile tests, fatigue tests were carried out

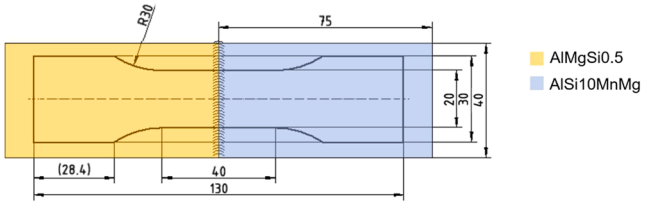

Fig. 4. Specimen geometry for characterization of laser welded joints via quasistatic tensile testing.

on an initial batch of samples. Compared to the specimens used for the tensile strength test, the specimens used for the fatigue evaluation are 5 mm wider, i.e., the width of the test cross-section is 25 mm. The S–N curve evaluation assumes a lognormal distribution in the fatigue life direction. Consequently, the S-N data are transformed using the base-10 logarithm. The S-N parameters are then determined by regression, treating load amplitude as the independent variable and fatigue life as the dependent variable. The scatter TS is computed from the standard deviation corrected by n-2, where n is the number of S-N data pairs.

The thickness of all specimens for mechanical testing corresponds to the thickness of the cast parts, which is 3 mm.

Results

Casting

Fig. 5 details the evolution of the phase fractions under equilibrium conditions of the AlSi10MnMg alloy variants under scrutiny as calculated by the JMatPro® software, following the compositions presented in Table 1. Accumulation of impurities or tramp elements as a result of recycled material content becomes an important aspect in industrial use of aluminum casting alloys since some elements are known for potentially detrimental effects on part properties. A typical, critical component in this respect is the β-Al_5FeSi phase, which can form plate-like structures acting as internal kerfs in the material. The thermodynamic simulations show which phases will be formed, in what proportions they will occur, and which of them appear first. Utilizing the fraction solid diagrams depicted in Fig. 5, the predicted phases display a progressive path during the solidification process: Liquid → Al_2Si_2M → Al_2Si_2M + α-Al → Al_2Si_2M + α-Al + Alpha → Al_2Si_2M + α-Al + Alpha + Silicon → Al_2Si_2M + α-Al + Alpha + Silicon + Mg_2Si. These phases mainly occupy the interdendritic regions surrounded by α-Al dendrites with a eutectic concentration of 85.98 wt.-% in terms of phase fraction.

The iron contents used in the simulations were based on the average values obtained via optical emission spectroscopy during the casting campaigns. The simulations demonstrate that increased levels of Fe in the alloys result in higher fractions of iron-containing phases such as α-$Al_{15}(Fe,Mn,Cr)_3Si_2$. These levels vary between 1,56 wt.-%, 2,17 wt.-% and 2,38 wt.-% from one alloy to another. Furthermore, the phases π-$Al_8FeMg_3Si_6$ and the aforementioned, critical ß-Al_5FeSi can be observed only within the recycled alloys, and at phase fraction below 1 wt.-%. However, occurrence of the latter phase is also controlled by the Fe/Mn ratio and the cooling and solidification rate. In our present study, the Fe/

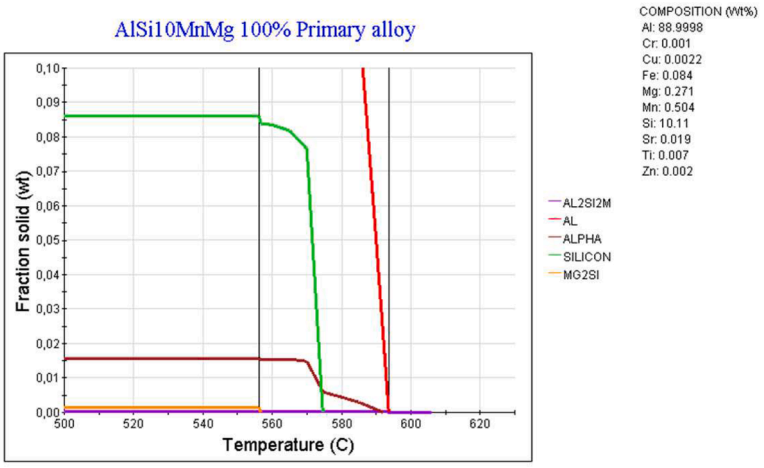

(a)

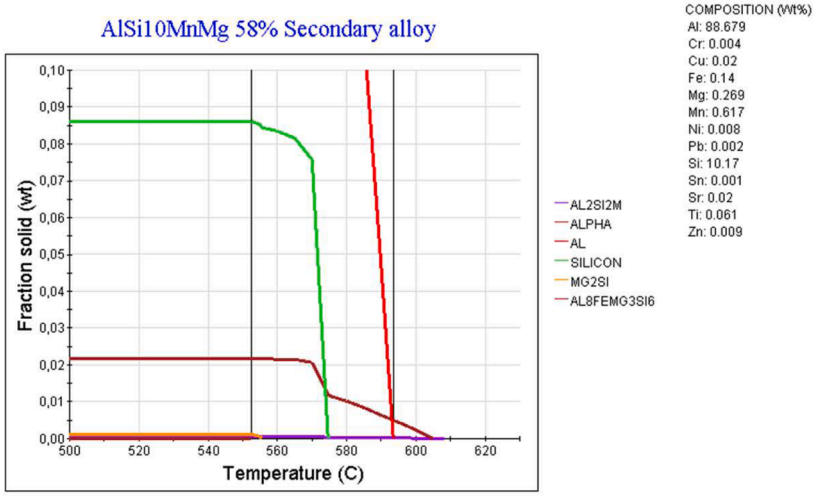

(b)

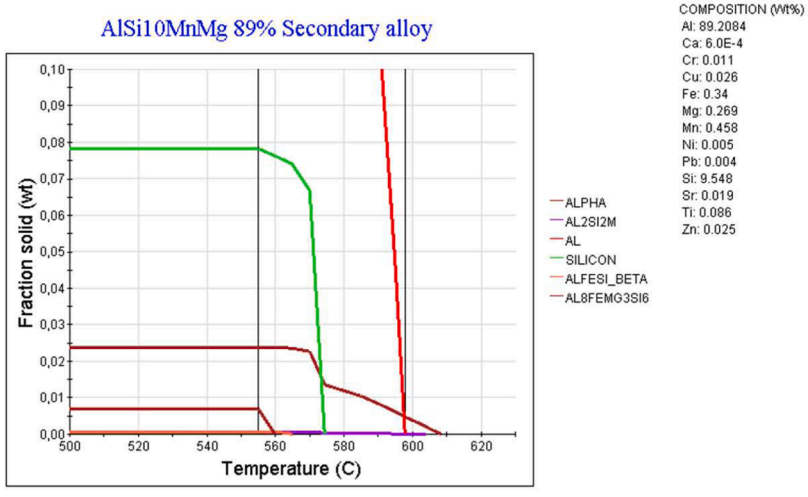

(c)

Fig. 5. The partial phase fraction vs. temperature plots through JMatPro® software showing detailed low fraction phases up to 0.10 wt.-% for the (a) AlSi10MnMg 100 wt.-% primary, (b) AlSi10MnMg 58 wt.-% secondary and (c) AlSi10MnMg 89 wt.-% secondary alloys for solidification under equilibrium conditions.

Mn ratio was 0.167 for the primary alloy, and 0.227 and 0.742 for the 58 wt.-% and the 89 wt.-% secondary alloy, respectively.

The typical microstructures resulting from the HPDC process are shown in Fig. 6 through optical images of unetched metallographic sections. All alloy variants show the typical microstructure of a refined AlSi10MnMg alloy. The different castings alloys are characterized by an α-Al matrix (primary Al mixed crystal, appearing light grey in Fig. 6) with a refined eutectic mixture in the interdendritic regions (mixture of grey and white). Furthermore, low fractions of α-$Al_{15}(Fe,Mn,Cr)_3Si_2$ can be observed (globular, medium grey, typically at interfaces between primary aluminum and eutectic phase). This confirms the predictions of the JMatPro® calculations in Fig. 5. The results of the metallographic examinations also show no significant differences between the primary AlSi10MnMg alloy and the variants with different secondary material levels within the domain accessible in terms of resolution via optical microscopy. The reader should note, though, that phase fractions below 1 wt.-% are unlikely to be detected in these micrographs: This includes the aforementioned β-Al_5FeSi phase. Since all alloy variants have an Sr content of approx. 200 ppm, i.e. they are refined, the fine variant of the Al-Si eutectic visible in the micrographs is formed. This refinement is usually also necessary in HPDC, as even the high cooling rates in die casting do not allow a sufficiently fine eutectic to be obtained and thus the desired high elongation values cannot be achieved without this measure.

Concerning melt preparation and the execution of the die casting trials, no substantial variations were observed in the process sequences among the different casting alloys. All specimens were produced at a cycle time of approximately 60 s and were quenched in water immediately after ejection from the die casting mold. The casting alloys exhibited excellent filling characteristics, low sticking tendency and no discernible visual differences in surface quality.

All samples cast were subjected to an X-ray radioscopy inspection were categorized into three quality levels: very good (class A – max. pore size $<$ 1 mm), good (class B – 1 mm $<$ max. pore size $<$ 2 mm) and adequate (class C - individual pores $>$ 2 mm and/or pore clusters) as depicted in Fig. 7. The alloy variant with the highest secondary material content showed a slightly reduced proportion of samples classified as either class A or Class B (Rohwer et al., 2024; Bleicher et al., 2025. Nevertheless, since an excellent density index of $<$1 % was achieved for this material in particular after melt treatment, the increased porosity observed in the cast components may either be attributable to differences in material composition, as this alloy contains the highest amount of iron in the comparison, or process-related fluctuations based on effects such as the manual application of the release agent. However, any effect of the latter type would not be relevant for the present results, as only class A samples were considered for the welding experiments.

Mechanical properties of the different alloys were established based on specimens cut from the dogbone samples. A detailed overview of this investigation including a study on the effects of casting defects has been undertaken. The results, however, show only limited differences between the different alloys and quality classes: In all cases, the average yield strength is almost entirely unaffected. Ultimate tensile strength is similar in class A and B, with higher levels measured for class B in the case of the two Aluminium Rheinfelden alloys, a pattern which is reflected in the elongation at failure data, too. However, all materials show a notable drop from class B to class C. It is thus assumed that either pores are too small or the total porosity levels remain below a critical threshold only the transgression of which might have an influence on quasistatic properties in class A and B, and that the deviation in UTS observed is mostly the consequence of statistical variation between samples. The respective data is summarized in terms of yield strength, ultimate tensile strength and elongation at failure in Table 6. Despite the limited deviations, for the welding experiments, only class A samples were chosen in order to avoid introducing possible secondary effects on the outcome.

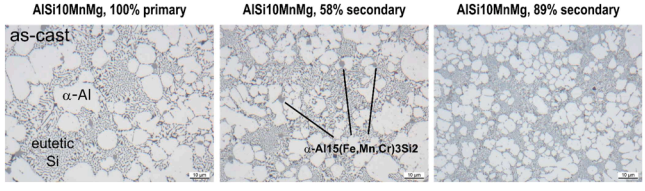

Fig. 6. Typical HPDC optical microstructures as revealed by flat metallographic sections stemming from the core of the AlSi10MnMg alloy castings detailing the phases formed.

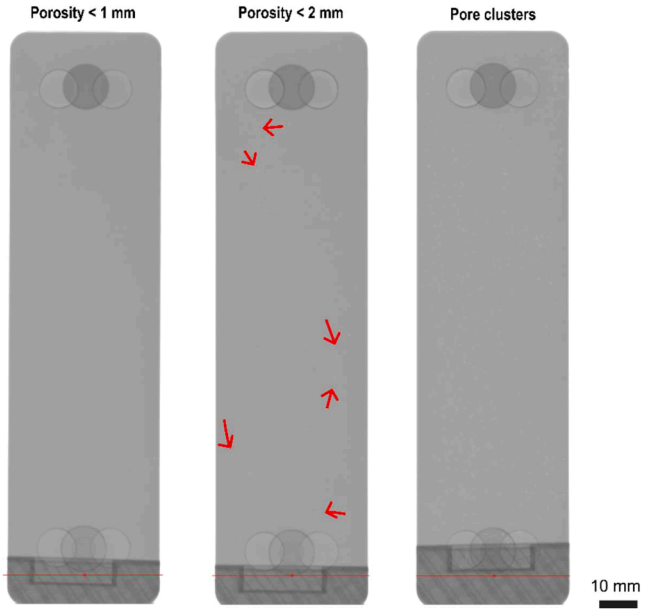

Fig. 7. X-Ray images of the die-cast aluminum components showing internal porosity distribution. Regions of low-density material, related to gas or shrinkage porosity, are visible as brighter areas. The samples were categorized as "very good" (max. pore size $<$ 1 mm), "good" (max. pore size $<$ 2 mm) and "adequate" (max. pore size $>$ 2 mm or pore clusters).

Table 6
Yield strength levels of the three alloy variants compared in this study for the three quality classes A, B and C. Despite the fact that the deviation in properties is limited between classes, only class A samples were used for the welding experiments.

Alloy variant	Property	Class A	Class B	Class C
100 % primary	Yield Strength [MPa]	142.5	139.0	137.7
	Std. Dev. [MPa]	5.26	1.73	3.79
	Ultimate Tensile Strength [MPa]	253.8	257.7	234.7
	Std. Dev. [MPa]	13.82	28.18	31.90
	Elongation at Failure [%]	3.20	4.1	2.7
	Std. Dev. [%]	0.94	2.03	1.23
58 % secondary	Yield Strength [MPa]	135.8	137.0	135.3
	Std. Dev. [MPa]	1.50	3.00	2.5
	Ultimate Tensile Strength [MPa]	254.5	274.0	247.5
	Std. Dev. [MPa]	28.39	2.65	24.47
	Elongation at Failure [%]	4.13	5.47	3.35
	Std. Dev. [%]	1.73	0.59	1.12
89 % secondary	Yield Strength [MPa]	138.3	141.0	141.3
	Std. Dev. [MPa]	2.08	1.15	1.50
	Ultimate Tensile Strength [MPa]	273.3	265.8	248.5
	Std. Dev. [MPa]	5.5	7.27	8.19
	Elongation at Failure [%]	5.23	4.35	3.1
	Std. Dev. [%]	0.29	0.66	0.51

Welding

Among the test series conducted, the weld seams produced using static beam guidance exhibited a high degree of porosity (see Fig. 8). Three different optical configurations were used for this variant of the welding process. Starting from a spot diameter comparable to that used later in the dynamic beam oscillation experiments (35 µm, 1.2 kW), one with 300 µm, comparable to the overall scan diameter, and one 300 µm spot with defined intensity distribution. In the latter case, a core (20 %) and ring (80 %) distribution was set at the same power (10 kW), see Fig. 8 for a complete overview. In contrast, experiments incorporating superimposed beam oscillation demonstrated a significant reduction in pore formation in certain cases. Between these, a clear trend of decreasing porosity with increasing oscillation frequency was observed.

At an oscillation frequency of 4000 Hz, a widening of the capillary is likely attributed to the high relative velocity of the laser beam and the relatively small process interaction zone, combined with the high intensity of the laser. At the mid-length of the capillary, the diameter varies by approximately 300 µm. These observations suggest that the high-frequency oscillation induces dynamic changes in the capillary and melt pool behavior, influencing the overall process characteristics, see Fig.8. For those samples, despite the presence of individual cavities in the initial state, the overall porosity was found to be low compared to conventional welding. Nevertheless, it was noted that a significant number of pores tended to form along the side of the die-cast material of the weld seam.

However, differences become apparent when the line energy varies, which is also visible in the cross section image of the fusion zone. If too little energy per unit length is applied (smallest volume), a larger number of fine pores is observed, while the lowest total pore volume is found at a medium energy per unit length level. One possible reason for this may be the amount of energy applied. The lower the energy, the smaller is both the melt pool volume and its surface area, and thus the less opportunity and time is available for degassing. As the energy per unit length is further increased, more die-cast material is melted. However, the time and energy required for degassing are no longer available, as is obvious from Fig. 9, which depicts both longitudinal and cross sections of the respective weld seams.

Having thus established optimized process conditions for dynamic beam oscillation, there were then transferred to the samples with secondary material content. The results are illustrated in Fig. 10. In the case of the material with 89 wt.-% secondary material fraction, samples produced using the same welding parameters also show smaller, but also occasionally larger diameter pores in the cross sectional image, which however represents an arbitrary perspective on the sample. Looking at the total pore volume determined for all three casting variants (also related in Fig. 10), the differences are relatively small. In addition, none of the welded samples showed any ejections.

If this result is compared with the static welding tests involving the primary alloy, it becomes clear that with the same energy input, the porosity is significantly better regardless of the recycled content of the aluminum alloy. From a process procedure perspective, there is therefore no reason to consider a degradation in weld seam quality with a higher aluminum recycling content.

Properties (Hardness, mechanical strength, fatigue)

Based on the successful solution approach of dynamic beam oscillation for the production of high-quality mixed joints of high pressure die cast and wrought aluminum, hardness and tensile tests – the latter under quasistatic and cyclic regimes - were carried out on classic bar specimens. The hardness mapping shows the hardness transition from the wrought alloy to the weld seam in the cast material in a cross section using color coding (see Fig. 11).

Corresponding to the hardness measurement, static tensile tests were performed and the failure location of the samples was determined. Despite the differences in recycling content of the AlSi10MnMg cast alloy, the static and tensile properties are comparable within the dispersion. Failure occurs in all variants within the degraded area of the AlMgSi0.5 extruded profile at the heat-affected zone (HAZ). Thus, due to the identical failure location from the perspective of static strength and achievable elongation, no disadvantage can be identified from the use of the secondary alloy component. The ultimate tensile strength of the class A cast materials was between 253.8 and 273.3 MPa across all alloys (determined experimentally, see Table 6), and for AlMgSi0.5, according to the material data sheet, 215–260 MPa (DIN EN 1706, 2021). Based on the welded joint with 0 % recycled content in the AlSi10MnMg melt, ultimate tensile strength was approximately 161 MPa ± 6.0 MPa, see Fig. 11. The material combinations with secondary material content achieved comparable strengths. Due to the heat input of the welding process next to the weld seam the solution heat treated and warm aged wrought alloy is losing both hardness and strength in relative to the original T66 state. The difference is clearly reflected by the hardness mapping, which covers both the HAZ and the unaffected region of the wrought alloy (see Fig. 11). In contrast to the wrought alloy, the cast material does not show a comparable, clearly distinguished HAZ.

The initial fatigue test results depicted in Fig. 12 show the plotted number of cycles. *N* refers to the number of cycles to fracture. In all

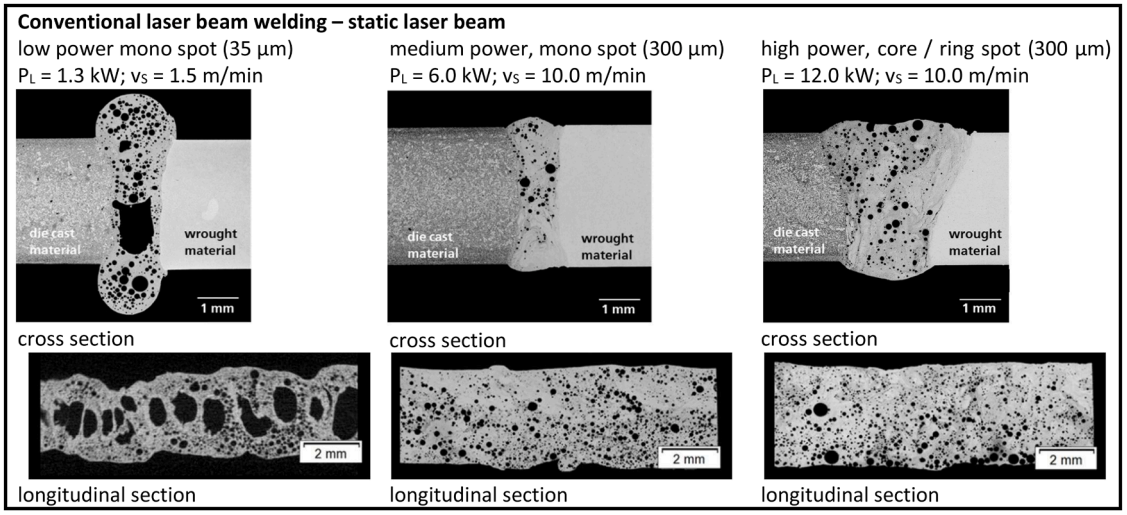

Fig. 8. Typical weld seam defects for laser welded aluminum die-cast material using conventional process parameter (static laser beam).

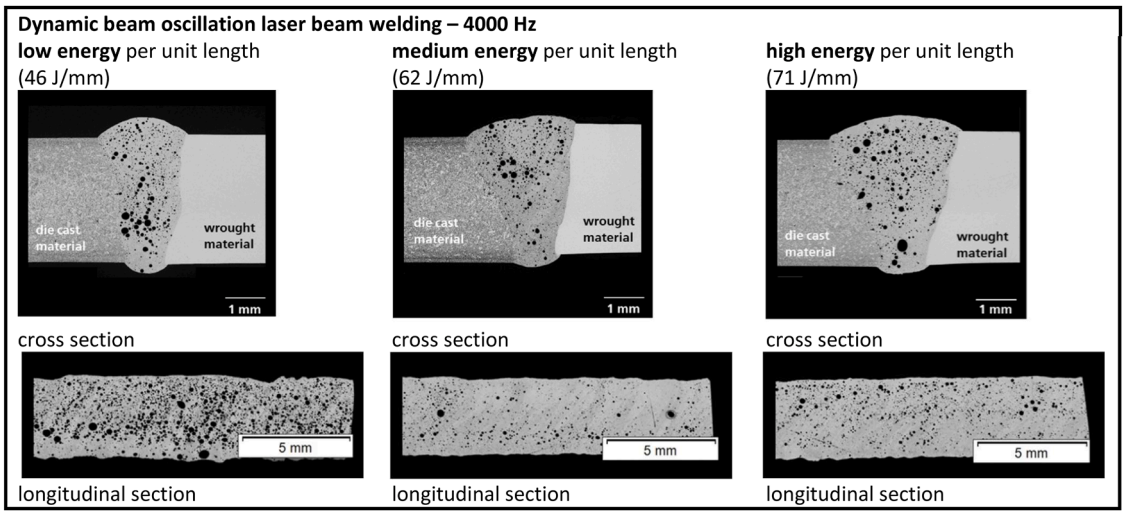

Fig. 9. Effect of dynamic beam oscillation on weld quality for laser welding of aluminum high pressure die cast material at different levels of energy per unit length: Significant reduction of porosity and smaller pore size obtained.

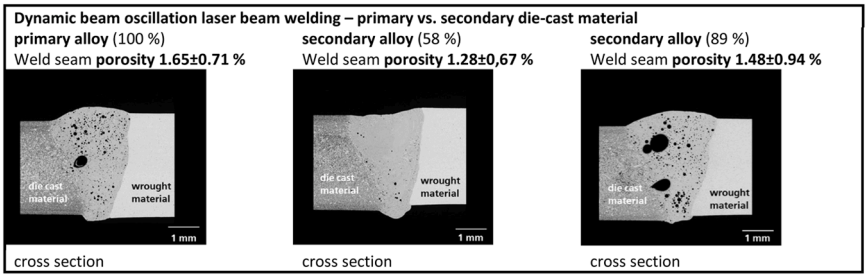

Fig. 10. Transfer of dynamic beam oscillation procedure to die-cast material with increasing secondary alloying amount – no tendency of weld seam quality degradation based on the secondary material content is observed.

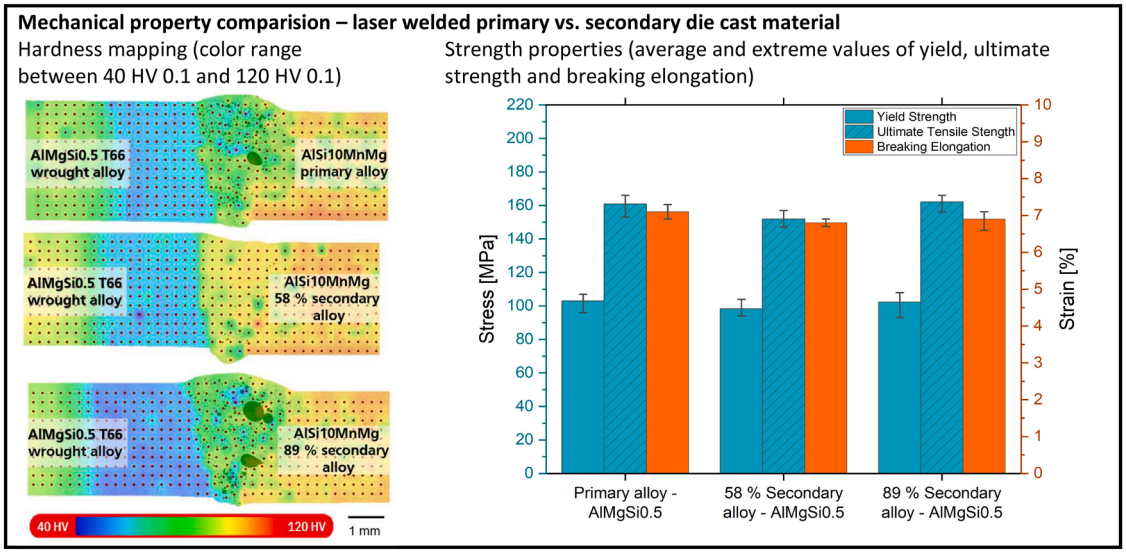

Fig. 11. Overview of mechanical properties of welded joints between primary and predominantly secondary aluminum high pressure die cast alloys of the AlSi10MnMg alloy family in combination with the wrought aluminum alloy EN AW-6060 (AlMgSi0.5) in T66 heat treatment state.

cases, failure occurred in the heat-affected zone directly at the weld toe on the die-cast plate side (AlSi10MnMg). Within the examined set, no systematic effect of alloy composition on the fatigue strength of the welds can be demonstrated due to the relatively small sample size. Most individual data points fall within a common scatter band. There is no evidence of a reduction in fatigue strength for secondary alloys. If anything, the secondary alloy tends to exhibit the highest fatigue strength.

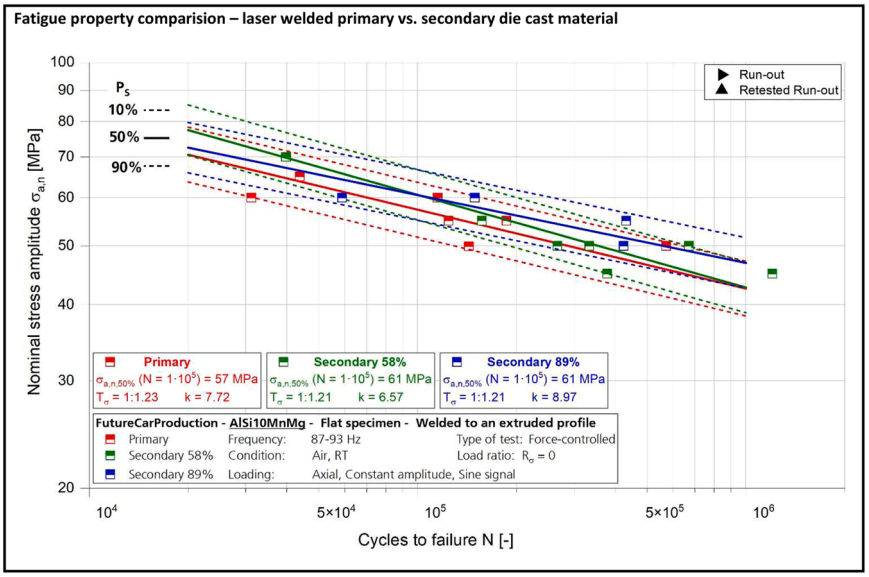

Fig. 12. Summary of fatigue test results for welded, unnotched specimens in the finite-life regime up to $N = 1 \bullet 10^6$ cycles.

Discussions

The experimental comparison of the samples without and with beam oscillation (Figs. 8 and 9) shows a clear reduction in the number of pores in the cross-section and longitudinal section due to the 2D beam movement. If the seam formation and the seam area produced are included in the discussion, the samples welded with a mono-spot show melt flanks that are almost parallel. As a result, the weld metal area produced is smaller, but the number of pores is greater than that of the samples with dynamic beam oscillation. Although less material is melted, the nominal pore volume is higher.

The reason for this is the reduced temperature gradient due to continuous over-welding caused by the oscillation superimposed on the feed direction. This prevents large pores from adhering to the melt line in the solidifying area, (see (Kamm et al., 2025)). In addition, the melt pool dynamics caused by the oscillation facilitates continuous degassing of the melt itself. Furthermore, the pores fluctuate in the melt for longer than it is possible in mono spot weld joints, which also supports degassing, (see (Börner et al., 2025)). Only small pores remain in the melt. These effects are further supported by the larger volume and surface area of the melt pool, which provides increased time and interface area for degassing.

The advantage of 2D beam oscillation appears to be independent of the additional alloying elements melted in the secondary material, see Fig. 5. Even recycled content of up to 89 % is qualitatively comparable in terms of measured porosity to joints with reduced or no secondary content. From a welding technology perspective, there is no reason not to use secondary castings for mixed joints with a classic wrought alloy. While this is visible in weld seam cross and longitudinal sections, the tensile test results cannot support this directly, as failure invariably occured in the HAZ of the wrought alloy, and thus any possible property variation of the weld seam and the HAZ in the cast part could not be captured by the quasistatic tensile tests. As a consequence, the data gathered can only provide a lower boundary for the strength of the weld seam itself. However, the aforementioned finding is supported by the fatigue curves depicted in Fig. 12, which are almost superimposed on each other, and it also matches the experiences gathered during the high pressure die casting experiments and the evaluation of the samples originating from these. As has been demonstrated via the mechanical property values reported in section 3.1, no significant differences in terms of mechanical properties were found despite the slight variation in phases present suggested by the JMatPro® simulations. Nevertheless, it remains a task for future investigations to close this knowledge gap by investigating joints between two high pressure die cast specimens. In terms of the fatigue test results, the observed change of the failure location from the HAZ of the wrought alloy to the transition between weld seam and HAZ in the cast alloy may also be explained by the thermal influence on the wrought material, which, while loosing strength, gained ductility. This change in material behavior is likely to influence crack propagation, leading to a situation in which the wrought alloy, even if showing lower yield and ultimate tensile strength than its cast counterpart in quasistatic tests, may fare better under cyclic loading conditions due to outmatching the casting terms of crack arrest characteristics. In this context, it is noteworthy that according to studies by Cinkilic et al., who scrutinized the formation of the notorious β-Al_5FeSi phase as a function of cooling rate and Fe/Mn ratio, the HAZ in the cast material should at least in the case of the Raffmetal alloy with 89 wt. % of secondary material and a Fe/Mn ratio of 0.742 be prone to formation of this phase the plate-like morphology of which is known to negatively affect fracture toughness and fatigue properties (Cinkilic et al., 2019).

Conclusion

In this study, a laser beam welding process for high pressure die cast in combination with wrought aluminum alloys was successfully validated. Furthermore, it was shown that no adjustment of the laser welding process parameters is necessary when transferring the process from primary die casting alloys to alloy variants with higher secondary aluminum content. This finding is in line with the observation that the high pressure die casting alloys of the AlSi10MnMg type studied here did not show any statistically significant deviations in terms of both casting characteristics and mechanical properties as function of secondary material content. The resulting weld seams have an extremely low porosity, with pore diameters of <0.3 mm and a total pore content of <2 %. This result underscores the suitability of the process as an efficient joining technique for the lightweight construction of automotive body parts. In the context of differential structural concepts, the technology has significant potential for the production of weight-optimized components. Since introduction of recycled materials affecting material compositions to the level seen in the present study had only negligible consequences, the data gathered can help pave the way for use of such materials in future applications of this type. This can also contribute to a reduction in CO_2 emissions during the production phase. Future investigations should extend the scope of the present study towards joints between two

high pressure die cast components, and might also look into the effect of flow length on weldability.

CRediT authorship contribution statement

Dirk Dittrich: Writing – review & editing, Writing – original draft, Visualization, Validation, Supervision, Project administration, Formal analysis, Data curation, Conceptualization. **Dirk Lehmhus:** Writing – review & editing, Writing – original draft, Visualization, Validation, Supervision, Methodology, Investigation, Formal analysis, Data curation, Conceptualization. **Marco Haesche:** Writing – original draft, Visualization, Methodology, Conceptualization. **Leonardo Fernandes Gomes:** Writing – review & editing, Writing – original draft, Visualization, Methodology, Investigation, Formal analysis, Data curation, Conceptualization. **Christoph Pille:** Writing – review & editing, Supervision, Project administration, Funding acquisition, Conceptualization. **Axel Jahn:** Supervision, Project administration, Investigation, Funding acquisition, Conceptualization. **Linda Ullmann:** Writing – original draft, Visualization, Methodology, Formal analysis, Data curation. **Charlotte Graner:** Writing – review & editing, Writing – original draft, Visualization, Validation, Methodology, Investigation, Formal analysis, Data curation.

Declaration of competing interest

The authors declare that they have no known competing financial interests or personal relationships that could have appeared to influence the work reported in this paper.

Acknowledgment

We would like to thank the Fraunhofer Gesellschaft for its financial support of this project in the frame of a “flagship project” with the title "FutureCarProduction". We would also like to express our special thanks to our project partners Fraunhofer IIS in Fürth (F. Sukowski) and Fraunhofer LBF (F.-Chr. Reissner) in Darmstadt as well as all other contribution Fraunhofer Institutes within the project and the participating industrial partners for their valuable cooperation and contribution to the success of this project.

Data availability

The authors do not have permission to share data.

References

Aluminiumlegierungen - Qualität für die industrielle Verarbeitung (2025). Available at: https://www.speira.com/de/aluminiumlegierungen (Accessed: 15 May 2025).

Ashtari, P., Tetley-Gerard, K., Sadayappan, K., 2012. Removal of iron from recycled aluminium alloys. Canadian Metallurgi. Quarter. 51 (1), 75–80. https://doi.org/10.1179/1879139511Y.0000000026. -01.

Bleicher, C., Qaralleh, A., Lehmhus, D., Haesche, M. et al., Aspects for the Optimization of Car Production Regarding Efficiency, Availability and Sustainability, SAE Technical 2025-01-8609, 2025,10.4271/2025-01-8609.

Börner, S., Dittrich, D., Mohlau, P., et al., 2021. In situ observation with x-ray for tentative exploration of laser beam welding processes for aluminum-based alloys. J. Laser Appl. 33 (1), 012026.

Börner, S., Dittrich, D., Barrios Laranaga, J., et al., 2023. Enhanced process understanding for laser welding of copper and aluminum alloys with dynamic beam oscillation. In: Proc. LiM. Munich, Germany.

Börner, S., Dittrich, D., Sahm, T., Ullmann, L., Kamm, P.H., Jahn, A., 2025. X-ray analysis of capillary and melt pool dynamics using laser beam oscillation welding for aluminum die-casts. J. Laser Appl. 37 (2), 022019. https://doi.org/10.2351/7.0001639, 1 May.

Burggräf, P., Bergweiler, G., Kehrer, S., Krawczyk, T., Fiedler, F., 2024. Mega-casting in the automotive production system: expert interview-based impact analysis of large-format aluminium high-pressure die-casting (HPDC) on the vehicle pro-duction. J. Manuf. Proces. 124, 918–935.

Cinkilic, E., Ridgeway, C.D., Yan, X., Luo, A.A., 2019. Formation map of iron-containing intermetallic phases in recycled cast aluminum alloys. Metallurgi. Mater. Trans. A 50, 5945–5956. https://doi.org/10.1007/s11661-019-05469-6.

De Caro, D., Tedesco, M.M., Pujante, J., Bongiovanni, A., Sbrega, G., Baricco, M., Rizzi, P., 2023. Effect of recycling on the mechanical properties of 6000 series aluminum-alloy sheet. Materials 16, 6778. https://doi.org/10.3390/ma16206778.

Dichte-Index, 2025. https://www.giessereilexikon.com/giesserei-lexikon/Encyclopedia/show/dichte-index-654/?cHash=bcc2f13577d42ce2c3569212bac80bb7 (Accessed: 30 June 2025).

DIN EN 1706 (2021). Aluminium and aluminium alloys - Castings - Chemical composition and mechanical properties. DIN Deutsches Institut für Normung e.V., Berlin.

DIN EN ISO 13919-1 (2020). Welding - Electron and laser beam welded joints — Guidance on quality levels for imperfections - Part 1: Steel. DIN Deutsches Institut für Normung e.V., Berlin.

Dittrich, D., Jahn, A., Standfuss, J., Beyer, E., 2017. Laser beam welding of atmosphere aluminum die-cast material using high frequency beam oscillation and brilliant beam sources. J. Laser Appl. 29, 022425.

Dittrich, D., 2019. Möglichkeiten Und Perspektiven für das Verbindungsschweißen von Druckgussbauteilen, 106. GIESSEREI, pp. 36–41.

Kamm, P.H., Börner, S., Neu, T.R., et al., 2025. Operando X-ray tomoscopy of laser beam welding. Adv. Sci. 12 (9), e2413108. https://doi.org/10.1002/advs.202413108.

Lee-Jones, S. (2022). Tesla’s Texas-made model Y body structure: 2 pieces versus 171 in Model 3. Available at: https://teslanorth.com/2022/04/20/teslas-texas-made-model-y-body-structure-2-pieces-versus-171-in-model-3/ (Accessed: 12 August 2025).

Lehmhus, D., 2022. Advances in metal casting technology: A review of state of the art, challenges and trends-Part I: changing markets, changing products. Metals 12, 1959. https://doi.org/10.3390/met12111959.

Lehmhus, D., 2024. Advances in metal casting technology: a review of state of the art, challenges and trends-Part II: technologies new and revived. Metals 14, 334. https://doi.org/10.3390/met14030334.

Letyagin, N.V., Akopyan, T.K., Palkin, P.A., Cherkasov, S.O., Lyukhter, A.B., Rechnikov, I.S., 2024. Laser welding of aluminum-calcium alloys based on ((Al)+Al4(Ca, La)) eutectic. Metallurgist 68 (5), 692–701. https://doi.org/10.1007/s11015-024-01775-6. -09.

Mikolajčika, M., Tillováa, E., Chalupováa, M., Kucharikováa, L., Šurdováa, Z., 2023. Effect of increasing Fe content on the fatigue resistance of secondary aluminium alloy AlSi7Mg0.6. Transport. Res. Proced. 74, 493–499. https://doi.org/10.1016/j.trpro.2023.11.173.

Peng, T., Ren, L., Du, E., Ou, X., Yan, X., 2022. Life cycle energy consumption and greenhouse gas emissions analysis of primary and recycled aluminum in China. Processes 10, 2299. https://doi.org/10.3390/pr10112299.

Prieto, C., Vaamonde, E., Diego.-Vallejo, D., Jimenez, J., Urbach, B., Vidne, Y., Shekel, E., 2020. Dynamic laser beam shaping for laser aluminium welding in e-mobility applications. Procedia CIRP 94, 596–600. https://doi.org/10.1016/j.procir.2020.09.084.

Rohwer, V., Krinke, S., Lehmhus, D., Pille, C., Fendt, D., 2024. Sustainable materials in automotive body engineering, the role of (Giga-) casting technology to meet net zero targets. In: Proceedings of the NADCA Congress and Exposition. Indianapolis, USA, 30.09.-02.10.

The International Aluminium Institute (2025). The Aluminium Story. Available at: http://www.thealuminiumstory.com (Accessed: 29 August 2025).